ChemComm

COMMUNICATION

View Article Online
View Journal | View Issue

Cite this: *Chem. Commun.*, 2024, **60**, 1325

Received 24th November 2023,
Accepted 2nd January 2024

DOI: 10.1039/d3cc05762c

rsc.li/chemcomm

Reduction of intracellular oxidative stress with a copper-incorporated layered double hydroxide†

Adél Szerlauth,[a] Tamara Madácsy,[b] Gergely Ferenc Samu,[c] Péter Bíró,[d] Miklós Erdélyi,[d] Gábor Varga,[e] Zhi Ping Xu,[f] József Maléth[b] and István Szilágyi*[a]

Biocompatible Cu(II)-doped layered double hydroxide (CMA) nanoparticles were developed to combat reactive oxygen species. The 2-dimensional nanozymes showed both superoxide dismutase- and catalase-like activities in chemical assays, while proving as efficient antioxidants in the reduction of intracellular oxidative stress. The results indicate the great promise of CMA in antioxidant therapies.

Reactive oxygen species (ROS) form in normal physiological processes and have important roles in redox signalling.[1] However, increased concentrations of ROS lead to oxidative stress and may cause serious problems in living organisms.[2,3] Enzymes (*e.g.*, superoxide dismutase (SOD) and catalase (CAT)) are the most efficient defence systems against ROS,[4] but their supplementation is complicated due to the presence of inhibitors, high sensitivity to the environmental conditions (*e.g.*, pH, temperature and light), and costly extraction, purification and storage.[5]

The application of nanozymes, *i.e.*, nanomaterials of enzyme-like activity, offers a potential alternative to replace natural enzymes in biomedical treatments and processes owing to their remarkable structural and functional stability as well as easy and economic preparation.[6] In the past decade, inorganic nanozymes with antioxidant activities have been extensively investigated to combat ROS.[7–11] Advantageous properties such as tuneable structure, biocompatibility and scalable production have made layered double hydroxides (LDHs) be a potential base for nanozyme development.[12,13] LDHs can be endowed with antioxidant activity by incorporating appropriate metal ions into the structure and hence, manganese-,[14] ruthenium-[15] and iron-[16] containing LDHs show peroxidase mimetic features, while LDHs modified with astaxanthine[17] or cobalt[18] possess remarkable SOD-like activity. On the other hand, copper-doped LDH composites are applied in cancer therapy.[19] Although significant progress has been made in the field, the development of LDH-based nanozymes of high structural and functional stability is still challenging. Besides, there is an urgent need for multifunctional (or broad-spectrum) antioxidant nanozymes, which are able to decompose different ROS simultaneously and hence, can be used as radical scavengers in antioxidant therapies. Due to the possibility of incorporation of different metal ions in their structures, LDH nanoparticles are promising candidates for such a task.

Herein, the development of a trimetallic 2-dimensional LDH (CMA) nanoparticle of SOD- and CAT-like activity is reported. The key step during synthesis was to partially replace Mg(II) ions with Cu(II) to endow the LDH nanoparticles with ROS scavenging activity. The structure of the obtained Cu(II)/Mg(II)/Al(III) LDH was studied using various spectroscopy, light scattering and microscopy techniques, while antioxidant activity was probed by enzymatic assays and on cell cultures. The CMA nanomaterials were highly efficient in decomposition of different ROS as well as in reduction of oxidative stress.

The details of the synthesis methods are described in the ESI.† The stoichiometric metal ion compositions of the samples were Mg_3Al, $Cu_{0.2}Mg_{2.8}Al$, $Cu_{0.4}Mg_{2.6}Al$ and $Cu_{0.6}Mg_{2.4}Al$, denoted as MA, CMA1, CMA2, and CMA3, respectively. First, the formation of LDHs was confirmed by X-ray diffraction (XRD) (Fig. 1(A)). The characteristic reflections of the LDH-type structure appeared;[16,20] however, a slight shift in the position of the (003) reflection was observed. The lattice parameters were calculated (see Table S1 in the ESI†). The basal

[a] *MTA-SZTE Momentum Biocolloids Research Group, Interdisciplinary Excellence Center, University of Szeged, H-6720 Szeged, Hungary. E-mail: szistvan@chem.u-szeged.hu*
[b] *MTA-SZTE Momentum Epithelial Cell Signaling and Secretion Research Group, Interdisciplinary Excellence Center, University of Szeged, H-6720 Szeged, Hungary*
[c] *Department of Molecular and Analytical Chemistry, University of Szeged, H-6720 Szeged, Hungary*
[d] *Department of Optics and Quantum Electronics, University of Szeged, H-6720 Szeged, Hungary*
[e] *Department of Applied and Environmental Chemistry, University of Szeged, H-6720 Szeged, Hungary*
[f] *Australian Institute for Bioengineering and Nanotechnology, The University of Queensland, QLD-4072 Brisbane, Australia*

† Electronic supplementary information (ESI) available: Experimental part and supporting data. See DOI: https://doi.org/10.1039/d3cc05762c

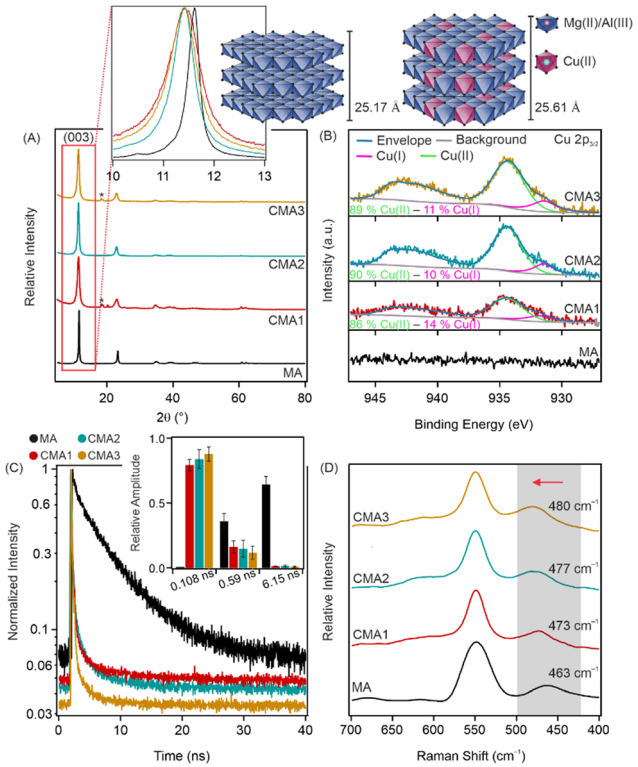

Fig. 1 XRD patterns (A), high resolution XPS spectra of the Cu $2p_{3/2}$ region (B), FLIM results (C) and Raman spectra (D) of MA, CMA1, CMA2, and CMA3 (from the bottom to the top, respectively). The schematic structures represent the increase in the *c* parameter due to the partial replacement of Mg(II) ions by Cu(II). The inset in (A) shows the (003) reflection in the range of 10–13°, while the inset in (C) shows the relative amplitude for the different fluorescence lifetime components. The grey shadow and red arrow in (D) show the shift of the peak at 463 cm^{-1}.

spacing (d(003)) and the *c* crystal parameter increased significantly for CMA samples compared to MA. The different d(003) and *c* values likely resulted from the partial replacement of Mg(II) ions by Cu(II), because the Jahn–Teller effect and the higher electronegativity of Cu(II) ions (compared to Mg(II)) can induce the distortion of the classical LDH structure.[21] Therefore, the incorporation of Cu(II) increased the layer thickness, leading to larger d and *c* values.

The hydrodynamic diameters of the LDH particles were determined in aqueous dispersions by dynamic light scattering being less than 100 nm in each case. The low polydispersity indices indicated a relatively narrow distribution of the particle size (Table S1 and Fig. S1, see ESI†). The zeta potential values were about +30 mV within the experimental error for all materials, *i.e.*, the surface charge did not change significantly by increasing the Cu(II) content in the LDHs (Table S1, ESI†).

The incorporation of Cu(II) ions into the positively charged layers was further explored by X-ray photoelectron spectroscopy (XPS). The CMA1, CMA2 and CMA3 surfaces were of similar chemical compositions and consisted of Mg, Al, C, O, and Cl. The presence of Cu was only slightly visible on the survey scans, indicating that only small amounts were incorporated into the LDH layers (Fig. S2, ESI†). The presence of Cu(II) was visible on the high resolution scans of sample CMA1-3 (Fig. 1B). The main Cu $2p_{3/2}$ line and the accompanying satellite feature could be fitted with the peaks of the $Cu(OH)_2$ compound[22] with a total of four components. The peaks were merged in the graph, but the individual binding energies (together with the literature reference) are indicated in Table S2 (ESI†). An additional peak was necessary to fit the low (931.75 eV) binding energy region indicating the presence of Cu(I) in the samples, which is in good agreement with former studies on Cu(II) containing LDHs.[19,23] However, it should be noted that the amount of Cu(I) was smaller compared to Cu(II). For both Al and Mg, only one chemical state was identified on the surface of the samples (Fig. S3, ESI†). Based on the binding energies, 49.4 eV for Mg–OH and 74.0 for Al–OH,[20] Mg(II) and Al(III) were identified on the surfaces. However, in the case of Al 2p, a large shift in the binding energies was observed (see Table S3 in the ESI†), most likely due to the change in the chemical environment upon incorporation of Cu(II) ions. The elemental composition of the surfaces was also determined by XPS measurements (Table S4, ESI†). The content of surface Cu(II) increased with increasing the Cu(II) amount during the synthesis method.

Fluorescence lifetime measurements (FLIMs) further confirm the incorporation of Cu(II) ions in the LDH structure (Fig. 1C). First, the arrival time distribution of the control sample (MA) was fitted with a double exponential model using the *n*-exponential deconvolution method, resulting in a long (6.15 ns) and a short (0.59 ns) component. Fitting the arrival time distributions of samples containing Cu(II) needed a tri-exponential model. Without fixing any parameters, two components were similar to the ones of the MA sample (a long and a short lifetime one) with a very short (<1 ns) third component. Based on this, the CMA distributions were refitted with two components fixed from the results of the MA sample. The fitted third component was identical for all three CMA samples (0.1 ns). It is worth noting here that the lifetime of the fitted third component equals the response time of the FLIM system. Therefore, one can assume that the real lifetime is even shorter, albeit it cannot be accurately determined. The fluorescent signal for LDH particles originates from the surface defects of the particles;[24] however, the metal ion ratio also affects the fluorescence properties of the LDH particles.[25] The above-explained change in fluorescence lifetime upon incorporation of Cu(II) is due to the different metal ion ratios in the LDH layers and also to the change in the number and position of surface defects on the surface of the particles.

Raman spectroscopy measurements were used to further explore structural aspects (Fig. 1D) of the compounds. The bands at 549 cm^{-1} and 463 cm^{-1} are related to the symmetric stretching vibrations of Al–O and Mg–O bonds, respectively, while the blue shift in the position of the latter peak indicates the partial substitution of Mg(II) by Cu(II) ions.[26]

The CAT-like activity of the CMA samples was assessed through H_2O_2 degradation tests, in which the reaction between H_2O_2 and ammonium molybdate leads to the formation of a yellow-coloured complex detected by a spectrophotometer. Then, the H_2O_2 (%) at different nanozyme concentrations was

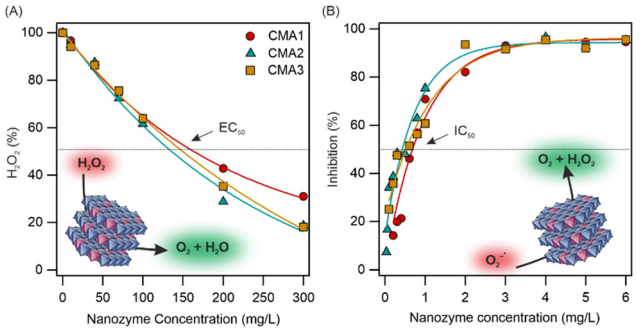

Fig. 2 The amount of H_2O_2 remaining after the CAT test reaction (H_2O_2 (%), see eqn (S3), ESI†) as a function of the initial nanozyme concentration (A) and the inhibition (eqn (S4), ESI†) as a function of the initial nanozyme concentration applied in the SOD assay (B).

calculated (Fig. 2A). A significant decrease was observed in the remaining amount of H_2O_2 by increasing the nanozyme concentration, indicating the CAT-like activity of the nanozymes. The EC50 values (Table S5, ESI†), *i.e.*, the concentrations needed to decompose half of the H_2O_2 in the reaction mixture, are very similar for all nanozymes and comparable to the native enzyme.[27] Thus, the CMA samples can be still considered as highly active CAT mimics.

To determine the SOD-like activity of the nanozymes, the Fridovich assay was applied (see details in the ESI†), during which superoxide radical ions ($O_2^{-\bullet}$), generated in the reaction of xanthine and xanthine oxidase, react with nitro blue tetrazolium (NBT) indicator molecules and cause a colour change in the reaction mixture that can be followed by using a spectrophotometer. The inhibition (eqn (S4), ESI†) of the NBT-$O_2^{-\bullet}$ reaction by the nanozymes was calculated. As shown in Fig. 2B, the maximum $O_2^{-\bullet}$ dismutation and the IC50 values were within the experimental error for all CMA compounds and did not show correlation to the amount of Cu(II)/Cu(I) incorporated (Table S5, ESI†). Similar to the CAT activity, the Cu(II)/Cu(I) content did not significantly affect the nanozyme activity, which remained similar for all three systems. While the obtained data indicate lower activity than the native SOD,[27] the nanozymes showed remarkable activity compared to similar nanomaterials published earlier in the literature.[28–30] To compare the SOD and CAT activity with other systems, the literature data are collected in Table S6 (ESI†). The MA samples were inactive in both enzymatic (CAT and SOD) assays (Fig. S4, ESI†); therefore, the catalytic activity clearly originated from the Cu(II)/Cu(I) centres in CMA1–3. Note that both Cu(II) and Cu(I) ions can act as SOD-like active centres, similar to the dismutation mechanism by the native SOD enzyme. However, based on the data obtained, one cannot unambiguously decide the extent of the individual contribution of these ions to the radical scavenging activity.

In addition, preliminary studies with a ROS/superoxide detection assay were carried out on cell cultures to select the optimal sample composition and concentration for further antioxidant activity measurements (Fig. 3A and B and Fig. S5, ESI†). To detect ROS/$O_2^{-\bullet}$ scavenging activity, menadione was

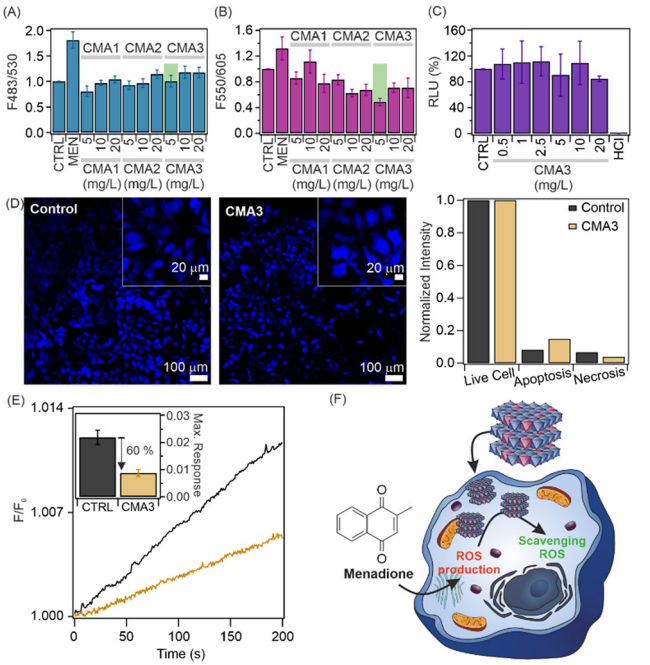

Fig. 3 Intracellular ROS (A) and $O_2^{-\bullet}$ (B) scavenging assays and CellTiter Glo assay for the CMA3 sample (C). Apoptosis/necrosis detection assays for 5 mg L^{-1} CMA3 samples (D). The bar graph shows normalized intensity of live/apoptotic/necrotic cells (D). Columns labelled CTRL are the negative control, while MEN and HCl are the positive controls. Changes in normalized fluorescence values (F/F_0) for untreated and CMA3-treated cells (E). Inset shows the maximum response for each system. Schematic representation of the activity of the CMA3 sample against menadione-induced intracellular ROS (F).

used to produce ROS, whereas ROS and $O_2^{-\bullet}$ were detected with green and orange fluorescence dyes, respectively. Based on the data of these studies, one can conclude that the activity of the nanozymes was within the experimental error in total ROS decomposition (Fig. 3A), while the 5 mg L^{-1} CMA3 sample showed the greatest activity in the intracellular $O_2^{-\bullet}$ scavenging assay (Fig. 3B).

The cell viability assessment was first determined for a wide range of nanoparticle concentrations using the CellTiter-Glo luminescent cell viability assay, as detailed in the ESI.† In brief, the test is based on adenosine triphosphate (ATP) production by the metabolically active cells, *i.e.*, the healthy cells are the ATP source for the luciferase reaction and produce a high luminescence signal. All three samples (Fig. 3C and Fig. S6, ESI†) showed high cytocompatibility at all applied concentrations. Therefore, based on the above findings, the sample conditions were chosen as 5 mg L^{-1} CMA3 dispersion for further studies.

More detailed apoptosis/necrosis assays were performed to visualize the cytocompatibility of CMA3 (Fig. 3D and Fig. S7, ESI†). HeLa cells were treated with the 5 mg L^{-1} CMA3 sample, after which apoptotic, necrotic, and healthy cells were labelled with Apopxin Green, 7-AAD and Cytocalcein Violet 450 fluorescent dyes, respectively. Apopxin Green detects the phosphatidyl serin moieties transferred to the outer plasma membrane,

while DNA strands in necrotic cells are detected using 7-AAD. Only a negligible amount of apoptotic or necrotic cells was seen in the fluorescence images. Thus, the results confirm the excellent cytocompatibility of CMA3 in the apoptosis/necrosis assays. The normalized fluorescence intensity values are shown in Fig. 3D.

Time-dependent ROS scavenging activity measurements were performed for a 5 mg L^{-1} CMA3 sample (Fig. 3E). Cells were treated with H2DCFDA, an ROS-sensitive fluorescent dye, and a 5 mg L^{-1} CMA3 sample. Upon menadione exposure to the cells, the fluorescence intensity increased steeply in the untreated cells, while a significantly smaller increase was observed in the treated cells due to the intracellular coexistence of CMA3, H2DCFDA and ROS. The inset represents the maximum responses and indicates that the intracellular ROS amount decreased by 60% after treatment with 5 mg L^{-1} CMA3. Thus, one can conclude that CMA3 is able to inhibit the development of ROS-induced oxidative stress (Fig. 3F).

In conclusion, the MA structure was systematically modified by partially replacing Mg(II) ions with Cu(II) ions, endowing the nanoparticles with enzyme-like properties. The nanozymes showed remarkable activity in H_2O_2 and $O_2^{-\bullet}$ decomposition in chemical test reactions, which was further revealed under intracellular conditions. The nanozymes did not show a cytotoxic effect on HeLa cells and were able to decrease the intracellular ROS and $O_2^{-\bullet}$ concentration significantly. Overall, the CMA3 sample showed the highest $O_2^{-\bullet}$ scavenging activity and could remarkably reduce intracellular oxidative stress. Thus, CMA3 is a promising antioxidant agent in medical therapies or other health preserving processes, wherever ROS decomposition is desired.

The authors are thankful for the support of the National Research, Development and Innovation Office (TKP2021-NVA-19 (I. S., M. E.) and TKP2021-EGA-28 (J. M.)), the Horizon Europe Marie Skłodowska-Curie Action (101086226), the Hungarian Academy of Sciences (LP2022-16/2022 (I. S.)), the Bolyai Research Fellowship (BO/00160/25/5 (T. M.)), the EU's Horizon 2020 research and innovation program under grant agreement No. 739593 (J. M.) and the University of Szeged Open Access Fund (6731).

Conflicts of interest

There are no conflicts to declare.

Notes and references

1 H. Sies and D. P. Jones, *Nat. Rev. Mol. Cell Biol.*, 2020, **21**, 363–383.
2 H. J. Forman and H. Q. Zhang, *Nat. Rev. Drug Discovery*, 2021, **20**, 689–709.
3 F. Ercole, C. J. Kim, N. V. Dao, W. K. L. Tse, M. R. Whittaker, F. Caruso and J. F. Quinn, *Biomacromolecules*, 2023, **24**, 387–399.
4 E. Mira, L. Carmona-Rodriguez, B. Perez-Villamil, J. Casas, M. J. Fernandez-Acenero, D. Martinez-Rey, P. Martin-Gonzalez, I. Heras-Murillo, M. Paz-Cabezas, M. Tardaguilal, T. D. Oury, S. Martin-Puig, R. A. Lacalle, G. Fabrias, E. Diaz-Rubio and S. Manes, *Nat. Commun.*, 2018, **9**, 575.
5 A. I. Benitez-Mateos, D. R. Padrosa and F. Paradisi, *Nat. Chem.*, 2022, **14**, 489–499.
6 M. Zandieh and J. W. Liu, *Adv. Mater.*, 2023, 2211041.
7 A. Martínez-Camarena, M. Merino, A. V. Sánchez-Sánchez, S. Blasco, J. M. Llinares, J. L. Mullor and E. García-España, *Chem. Commun.*, 2022, **58**, 5021–5024.
8 Y. X. Xing, L. Li, Y. H. Chen, L. Wang, S. Q. Tang, X. Y. Xie, S. Wang, J. X. Huang, K. Y. Cai and J. X. Zhang, *ACS Nano*, 2023, **17**, 6731–6744.
9 X. H. Niu, X. Li, Z. Y. Lyu, J. M. Pan, S. C. Ding, X. F. Ruan, W. L. Zhu, D. Du and Y. H. Lin, *Chem. Commun.*, 2020, **56**, 11338–11353.
10 C. Murugan, N. Murugan, A. K. Sundramoorthy and A. Sundaramurthy, *Chem. Commun.*, 2019, **55**, 8017–8020.
11 W. H. Gao, J. Y. He, L. Chen, X. Q. Meng, Y. N. Ma, L. L. Cheng, K. S. Tu, X. F. Gao, C. Liu, M. Z. Zhang, K. L. Fan, D. W. Pang and X. Y. Yan, *Nat. Commun.*, 2023, **14**, 160.
12 T. T. Hu, Z. Gu, G. R. Williams, M. Strimaite, J. J. Zha, Z. Zhou, X. C. Zhang, C. L. Tan and R. Z. Liang, *Chem. Soc. Rev.*, 2022, **51**, 6126–6176.
13 L. X. Zhang, J. Hu, Y. B. Jia, R. T. Liu, T. Cai and Z. P. Xu, *Nanoscale*, 2021, **13**, 7533–7549.
14 X. T. Yang, X. Cao, Y. Fu, J. Lu, X. T. Ma, R. Li, S. Y. Guan, S. Y. Zhou and X. Z. Qu, *J. Mater. Chem. B*, 2023, **11**, 1591–1598.
15 B. Q. Wang, Y. Y. Fang, X. Han, R. T. Jiang, L. Zhao, X. Yang, J. Jin, A. J. Han and J. F. Liu, *Angew. Chem., Int. Ed.*, 2023, e202307133.
16 Y. P. Ning, Y. Sun, X. Yang, Y. P. Li, A. J. Han, B. Q. Wang and J. F. Liu, *ACS Appl. Mater. Interfaces*, 2023, **15**, 26263–26272.
17 X. T. Ma, B. R. Zhang, N. Ma, C. X. Liu, Y. Miao, X. Liang, S. Y. Guan, D. W. Li, A. H. Liu and S. Y. Zhou, *ACS Appl. Mater. Interfaces*, 2023, **15**, 13869–13878.
18 S. Zhang, J. Chen, W. S. Yang and X. Chen, *Nano Res.*, 2022, **15**, 7940–7950.
19 L. Y. Sun, J. J. Wang, J. P. Liu, L. Li and Z. P. Xu, *Small Struct.*, 2021, **2**, 2000112.
20 G. Zhang, L. Wu, A. T. Tang, B. Weng, A. Atrens, S. D. Ma, L. Liu and F. S. Pan, *RSC Adv.*, 2018, **8**, 2248–2259.
21 J. S. Wu, Y. K. Xiao, J. Y. Wan and L. R. Wen, *Sci. China: Technol. Sci.*, 2012, **55**, 872–878.
22 M. C. Biesinger, *Surf. Interface Anal.*, 2017, **49**, 1325–1334.
23 B. Li, J. Tang, W. Y. Chen, G. Y. Hao, N. Kurniawan, Z. Gu and Z. P. Xu, *Biomaterials*, 2018, **177**, 40–51.
24 K. L. Xu, Z. Zhang, G. M. Chen and J. Q. Shen, *RSC Adv.*, 2014, **4**, 19218–19220.
25 R. Tian, D. Yan and M. Wei, in *Photofunctional Layered Materials*, ed. D. Yan and M. Wei, Springer International Publishing, Cham, 2015, pp. 1–68.
26 L. G. Dou and H. Zhang, *J. Mater. Chem. A*, 2016, **4**, 18990–19002.
27 A. Szerlauth, Á. Varga, T. Madácsy, D. Sebők, S. Bashiri, M. Skwarczynski, I. Toth, J. Maléth and I. Szilagyi, *ACS Mater. Lett.*, 2023, **5**, 565–573.
28 J. Y. Zeng, C. P. Ding, L. Chen, B. Yang, M. Li, X. Y. Wang, F. M. Su, C. T. Liu and Y. J. Huang, *ACS Appl. Mater. Interfaces*, 2023, **15**, 378–390.
29 Y. Zhang, L. X. Chen, R. M. Sun, R. J. Lv, T. Du, Y. H. Li, X. M. Zhang, R. T. Sheng and Y. F. Qi, *ACS Biomater. Sci. Eng.*, 2022, **8**, 638–648.
30 X. Y. Liu, D. X. Li, Y. Liang, Y. Lin, Z. X. Liu, H. T. Niu and Y. H. Xu, *J. Colloid Interface Sci.*, 2021, **601**, 167–176.

